ANTIOXIDANTS & REDOX SIGNALING
Volume 11, Number 8, 2009

DOI: 10.1089/ars.2009.2635

Forum Original Research Communication

Remodeling of the Ischemia-Reperfused Murine Heart: 11.7-T Cardiac Magnetic Resonance Imaging of Contrast-Enhanced Infarct Patches and Transmurality

Surya C. Gnyawali, Sashwati Roy, Molly McCoy, Sabyasachi Biswas, and Chandan K. Sen

Abstract

Our laboratory has published the first evidence obtained from fast low-angle-shot cine magnetic resonance imaging (11.7 T) studies demonstrating secondary myocyte death after ischemia/reperfusion (IR) of the murine heart. This work provides the first evidence from 11.7-T magnet-assisted pixel-level analysis of the post-IR murine myocardial infarct patches. Changes in function of the remodeling heart were examined in tandem. IR compromised cardiac function and induced LV hypertrophy. During recovery, the IR-induced increase in LV mass was partly offset. IR-induced wall thinning was noted in the anterior aspect of LV and at the diametrically opposite end. Infarct size was observed to be largest on post-IR days 3 and 7. With time (day 28), however, the infarct size was significantly reduced. IR-induced absolute signal-intensity enhancement was highest on post-IR days 3 and 7. As a function of post-IR time, signal-intensity enhancement was attenuated. The threshold of hyperenhanced tissue resulted in delineation of contours that identified necrotic (*bona fide* infarct) and reversibly injured infarct patches. The study of infarct transmurality indicated that whereas the permanently injured tissue volume remained unchanged, part of the reversibly injured infarct patch recovered in 4 weeks after IR. The approach validated in the current study is powerful in noninvasively monitoring remodeling of the post-IR beating murine myocardium. *Antioxid. Redox Signal.* 11, 1829–1839.

Introduction

Reperfusion of the ischemic myocardium is aimed at reducing myocardial dysfunction and improving tissue survival. Reperfusion, however, also poses the threat of tissue injury. Reperfusion injury may be broadly viewed as having two major components: oxidant-induced myocardial tissue damage during the reperfusion process, and progressive tissue damage secondary to the initial insult. We previously reported that acute myocardial infarction is followed by activation of myocyte death in the surviving portion of the heart (33). Remodeling of the heart after ischemia/reperfusion (IR) has a major impact on the survival of patients who have had a myocardial infarction. Understanding of post-IR myocardial remodeling is therefore critically important. The use of noninvasive technologies for such studies allows the repeated measure of the same heart in an experimental setting, providing powerful longitudinal data.

Left ventricular (LV) remodeling, after IR injury, is associated with changes in LV geometry, function, and histologic characteristics that lead to increased risk of heart failure and death (29, 34). Cardiac magnetic resonance imaging (MRI) is a well-established clinical tool commonly used to monitor the infarcted heart (28, 48). MRI enables the noninvasive repeated-measures assessment of the anatomy and physiology of the infarcted heart (19, 24). The advent of high-field-strength, small-bore magnets has enabled high-resolution MRI of the IR rodent heart. Recently, our laboratory published the first evidence obtained from fast low-angle-shot (FLASH) cine MR-imaging studies using an 11.7-T magnet to track secondary myocyte death after IR of the murine heart (33). Myocardial delayed contrast-enhancement imaging represents a versatile

Davis Heart & Lung Research Institute, Department of Surgery The Ohio State University Medical Center, Columbus, Ohio.

tool to assess regional contractile function and myocardial viability (13, 49). An inversion-recovery FLASH sequence, with gadolinium diethylenetriamine pentaacetic acid (Gd-DTPA) as the contrast agent, enables the visualization of IR-induced myocardial infarction (35, 36, 43), as well as of specialized anatomic abnormalities, such as left ventricular apical ballooning (4, 5, 35) in large animals and humans.

Whether delayed hyperenhancement is specifically limited to dysfunctional but viable myocardium or to reversibly injured regions surrounding the acute infarct tissue as well remains unclear (24). In this study, we sought to address this issue by pixel-level analysis of the scar tissue and tandem assessment of heart function. Such analysis of contrast-enhanced inversion-recovery MR images enabled the visualization of hyperenhanced and moderately enhanced patches in murine post-IR heart. The findings reported represent the first evidence from 11.7-T high-field-strength imaging of post-IR myocardial patches. High-resolution images generated by such an approach enabled, for the first time, pixel-level analysis of the IR murine heart at multiple time points after reperfusion. Murine cardiac cine-FLASH sequences were optimized for the measurement of functional parameters such as left ventricular chamber volumes (end-diastolic, end-systolic, stroke), ejection fraction (EF), cardiac output (CO), and LV mass.

Materials and Methods

Animal preparation and left anterior descending artery occlusion

Male C57BL/6 adult mice (8-week-old; 24.5 ± 1.5 g, mean $\pm$ SD; Harlan Technologies, IN) were maintained under standard laboratory housing conditions with access to chow and drinking water *ad libitum*. Ischemia/reperfusion of mice was performed as described earlier (33, 38). In brief, mice were anesthetized by using IP injection of a mixture of ketamine (50 mg/ml) and xylazine (10 mg/ml), laid on a warm surgical table, and intubated endotracheally. The mice were ventilated with a device (Harvard Apparatus, Boston, MA) on an air-isoflurane at an appropriate rate and tidal volume. Cardiac electrophysiology was monitored throughout the surgery by using a three-lead ECG setup, and changes were recorded by using PC Powerlab software (AD Instruments). The heart was accessed *via* left thoracotomy. The left lung was retracted to allow entrance to the pericardium. The left auricle was elevated to expose the coronary left anterior descending (LAD) artery, which was isolated by using 7-0 silk suture with a tapered needle. The suture was tightened over a piece of PE-10 tubing to induce reversible ischemia. LAD was occluded for 60 min. After 60 min, the suture was released to allow reperfusion in the injured myocardium. On successful reperfusion, the thorax was closed with interrupted 7-0 nylon sutures, as well as the skin incision with 5-0 polypropylene (Prolene) sutures. Throughout the surgery, body temperature was maintained at $36.7 \pm 0.5^{\circ}$C by using a heated surgical table and monitored with a rectal thermal probe. The ischemia episode was observed with pale coloration of LV myocardium. Thorax was closed, sutured, and the tracheal tube was disconnected, enabling the mouse to breathe on its own. The animal was then returned to its cage and placed on a heating block set to 37°C. Once the recovery was complete, the animal was returned to the rodent vivarium unit before the MRI experimental procedure. Mice were killed for harvesting the heart tissue after MR imaging, according to a standard protocol. All procedures were approved by the Institutional Laboratory Animal Care and Use Committee (ILACUC) of the Ohio State University.

Image acquisition

Baseline MR images ($n = 5$) were obtained 3–5 days before the surgery to allow sufficient time for recovery. After IR surgery, longitudinal repeated measures (post-IR days 3, 7, 14, and 28) were performed for the same mouse over time, such that each mouse served as its own control (paired baseline data). During the MRI, mice were anesthetized by using 1.5% isoflurane in a 95% oxygen and 5% carbon dioxide mixture. Mice were then positioned prone in a custom-manufactured animal holder, as reported previously (33). A custom-designed cradle was used to position the mouse vertically in the magnet. The cradle consisted of a nose-cone, lines for delivering and scavenging anesthetic gases, temperature control and electrocardiography (ECG) leads, and a respiratory monitoring system. Body core temperature was maintained at 37°C by using a specifically designed warm-air blower. ECG coupled with a respiratory gating device (Small Animal Instruments, Inc., Stony Brook, NY) was used for monitoring cardiac and respiratory signals derived from two needles inserted subcutaneously in the front-left and rear-right paws. Mice were secured within the holder by using surgical tape, without compressing their abdomen and chest regions.

MRI was performed by using a Bruker 11.7-T (500 MHz) MR microimaging system, which consists of a vertical magnet of bore size 30 mm (Bruker Biospin, Ettlingen, Germany). Quadrature-driven birdcage coils with inner diameters of 25 mm (Bruker Biospin) were used to transmit/receive the MR signals. In brief, mice were imaged by using a 30-mm proton-imaging probe. Tuning and matching the probe, slice-selective shimming and flip-angle calibration were performed manually before each experiment. Scout imaging for long- and short-axis orientation of the heart, by using a k-space segmented cardiac-triggered and ECG-gated gradient-recalled echo (GRE) fast low-angle shot (FLASH) sequence were performed. Six to seven contingent slices (slice thickness, 1 mm) were then acquired in short-axis orientation covering the entire heart. The imaging parameters were as follows: FOV (30×30 mm); matrix size, 256×192 (256×256 reconstructed postimaging); TE/TR, 1.43/8 ms; NEX, 4 to 6, a gaussian excitation pulse was applied for all chronically failing mouse hearts for the first data set of each normal mouse followed by post–time point assessment experiments.

After the ECG R-wave trigger pulse, images were collected at a frequency of 8 to 10 ms, such that 16 images were collected for each cardiac cycle, which lasts approximately 150 ms. Breath holding was achieved by acquiring images within short acquisition times, which produced images that were comparatively free of motional artifact from cardiac or respiratory movement. The fast acquisition times also allowed images of the entire thorax to be obtained during a single breath-hold. Controlling the contingent supply of the air–anesthesia mixture also helped minimize respiratory-motion artifacts. Because only a single line of the image can be acquired for K-space filling in each cardiac cycle, data from multiple heartbeats were acquired to form a complete image.

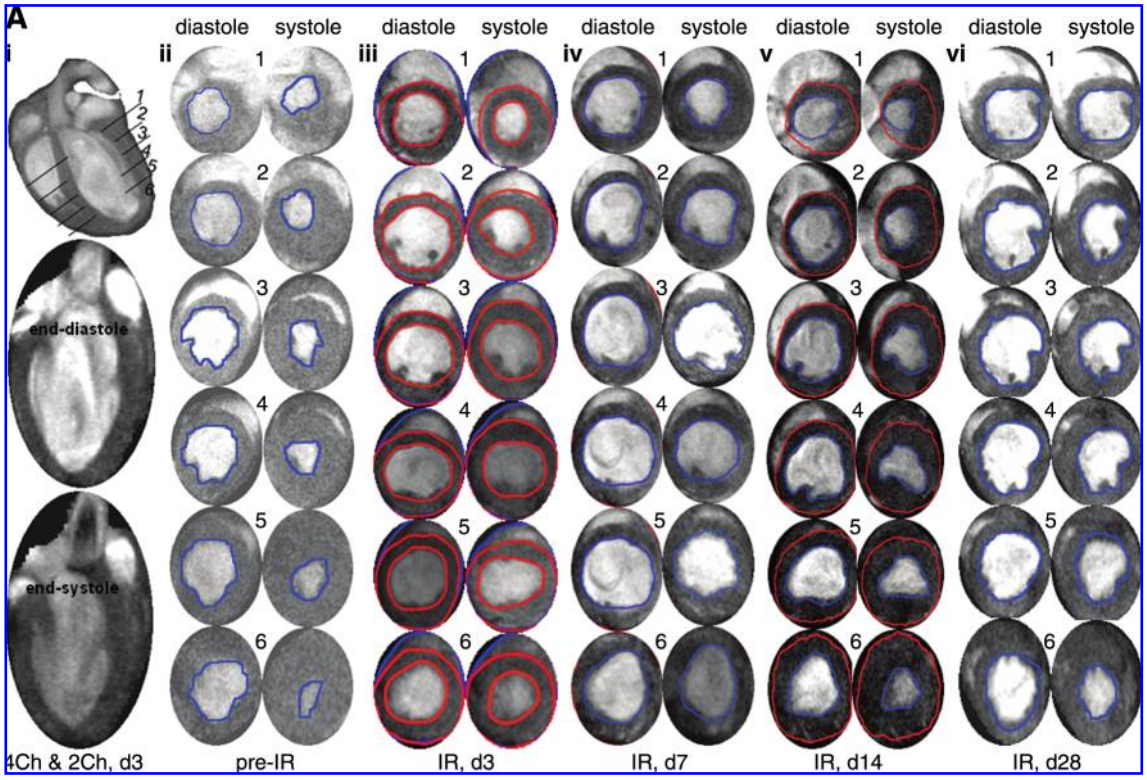

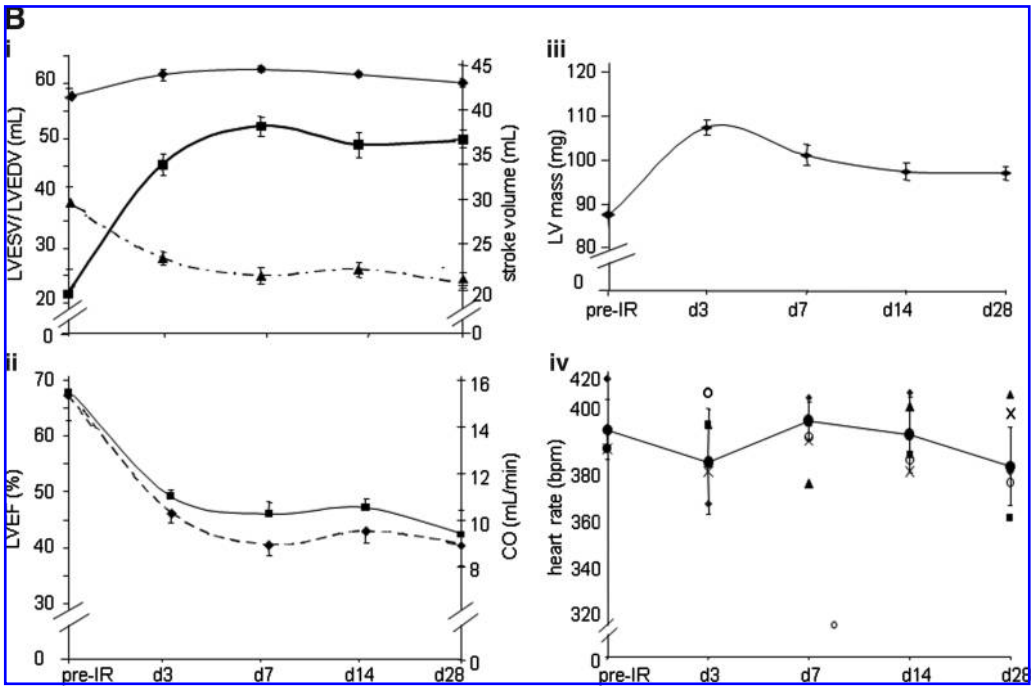

FIG. 1. Murine heart function after ischemia/reperfusion. (**A**) (**i**) top: long-axis four-chamber view showing six (1–6) axial imaging planes; center bottom: two chamber views: end diastole (center) and end systole (bottom); (**ii–vi**) short-axis image series for each of the six planes shown in **i** (*top*). Sixteen frames were imaged per cardiac cycle by using white blood FLASH. Sequence: TR ~160 ms; TE = 1.34 ms; FA = 15 degrees. (**B**) Quantitative illustration of observations made in (**A**). (**i**) All volumes are presented in one plot with two vertical axes (*left*, EDV and ESV; *right*, SV). The *thin curve* represents EDV (*top, diamond*); the *thick curve*, ESV (*middle, solid rectangle*); and the *dashed curve* (*bottom, solid triangle*) corresponds to SV. (**ii**) Heart functional parameters: EF (*top, solid curve*) and CO (*bottom, dotted curve*). (**iii**) Left ventricular mass; (**iv**) heart rate (beats per minute; bpm). Data represent mean ± SEM. Statistical treatment of data is presented in Table 1. IR, ischemia/reperfusion; LV, left ventricle; TR, repetition time; TE, echo time; FA, flip angle. (For interpretation of the references to color in this figure legend, the reader is referred to the web version of this article at www.liebertonline.com/ars).

Table 1. Statistical Treatment for Fig. 1B Addressing Cardiac Function

	LVEDV	*LVESV*	*SV*	*LVEF*	*CO*	*LV Mass*
pre vs d3	*	***	***	***	***	***
pre vs d7	*	***	***	***	***	***
pre vs d14	*	***	***	***	***	***
pre vs d28	*	***	***	**	**	**
d3 vs d7	ns	ns	ns	ns	ns	ns
d3 vs d14	ns	ns	ns	ns	ns	***
d3 vs d28	ns	ns	ns	ns	*	***
d7 vs d14	ns	ns	ns	ns	ns	ns
d7 vs d28	ns	ns	ns	ns	ns	ns
d14 vs d28	ns	ns	ns	ns	ns	ns

*$p < 0.05$.
**$p < 0.01$.
***$p < 0.001$.
ns, not significant different.

Signal averaging was used to enhance the signal-to-noise-ratio (SNR) and to minimize motion artifacts. The MR sequence used consisted of a radiofrequency (RF) pulse that excited the magnetization and gradient waveforms that spatially modulated the magnetization for image acquisition. The repetition time (TR) and echo time (TE) for GRE were chosen to be as short as possible to improve the temporal resolution and to allow more heart phases to be captured during the cardiac cycle. The flip angle of the excitation RF pulse used to acquire the image was 15 degrees. A single-slice acquisition was obtained in 2–3 min, depending on relevant imaging parameters (*i.e.,* matrix size and number of signal averages). The imaging time was estimated by multiplying the duration of the R–R interval of the ECG with the image matrix size and the number of signal averages. All animals were killed after MRI, and tissue was collected for histologic studies. All procedures were approved by the Institutional Laboratory Animal Care and Use Committee (ILACUC) of the Ohio State University.

MR contrast enhancement for infarct imaging

To discriminate between viable and nonviable myocardial tissue in the infarct region, delayed-contrast enhancement (DCE) was performed on a separate group of C57BL/6 mice ($n = 4$; time points: baseline and post-IR days 3 and 28). Gadolinium diethylenetriamine pentaacetic acid (Gd-DTPA; IP injection, 0.1–0.2 mmol/kg) was used as the contrast agent. Gd-DTPA shortens the T_1 (spin-lattice) relaxation time of the tissue (43). T_1-weighted images were acquired 20–30 min after contrast injection to detect the post-IR nonviable myocardium, which appears hyperintense because of the diffusion and retention of contrast agent into the site of the injury. Before image acquisition, an inversion RF pulse was applied, which inverted the tissue magnetization. The magnetization recovered at a rate corresponding to the T_1 time of the specific tissue. An inversion time (TI) of 300 ms was used to match the time at which the magnetization for normal myocardium nulls. At this time, the maximal contrast between viable and nonviable myocardium was achieved in murine heart. The optimal TI for DCE imaging can vary with the type of contrast agent, its concentration, and the field strength of the magnet. Proper selection of TI is important, as the contrast of the image can significantly vary, based on the choice of TI (8, 12, 42). A large flip angle (60 degrees) and a long TR (1,000 ms at 11.7 T) of 2 to 3 times the T_1 of normal myocardium with signal averages of 6 were used to maximize signal per acquisition. Because of the long TR, the total time needed to acquire a DCE image with an adequate spatial resolution was 10–12 min per acquisition. To image the entire left ventricle, a multislice acquisition (six slices of slice thickness 1.2 mm) technique was applied.

Image processing

LV function and mass. MR images were converted to DICOM format, as reported previously (33). A stack of short-axis image slices was acquired (thickness, 1.0 mm), fully covering the LV (planned at end-diastole) from the very base to the apical point. After the end-diastolic and end-systolic phases were identified on a slice-by-slice basis, the endocardial and epicardial borders were traced. LV end-systolic volume (ESV), LV end-diastolic volume (EDV), LV stroke volume (SV), cardiac output (CO), and LV ejection fraction (EF) were computed based on the traced borders. LV mass was calculated by slice summation by using the cardiac NMR (local software package), taking a specific gravity of 1.05 g/cc. LV mass was measured, including the most basal image slice and papillary muscles.

LV wall-thickness measurement. Left ventricular epi- and endocardium were delineated in all data sets. Image analyses were performed off-line by using *Segment* software (http://segment.heiberg.se) (15). Two slices were selected from the midventricular level of each heart for analysis of regional contractile function (11). The midventricular level was chosen because the infarct pattern in this region typically includes all three tissue types of interest (*i.e.,* enhanced, adjacent, and remote) (44). Slices closer to the base of the heart contain typically no or less infarct, whereas slices closer to the apex are nearly circumferentially infarcted. The circumference of each short-axis slice was divided into 18 equiangular radial segments, each of 20 degrees, taking right ventricular (RV) corner as the starting point, with clockwise rotation, as shown in the representative images (Fig. 2A). Papillary muscles were excluded in the endocardial borders during planimetry.

Infarct measurement. Delayed contrast-enhanced MR images were converted to DICOM format and transferred to Segment v1.8 R0670 software for infarct analysis. Images were processed pixel-wise by using Para-Vision PV4.0 software for infarct area, volume, and signal-intensity analysis. At each short-axis slice position, the end-diastolic phase was selected for infarct analysis. Image contrast and brightness were adjusted to nullify the noninfarcted myocardium while maximizing signal in the contrast-enhanced infarcted region. In the contrast-enhanced images, endocardial and epicardial borders as well as the borders of the signal-enhanced region were then subjected to planimetry. At each slice position, the number of enhanced and nonenhanced pixels was determined by using PV4.0. The size of the contrast-enhanced region was then expressed as a ratio of infarct to LV myocardial volume for all time points (Fig. 4ii). Scar size was assessed by using planimetry on each short-axis slice. Delineation of the hyperenhanced area followed by summation of data from each slice resulted in volume determination.

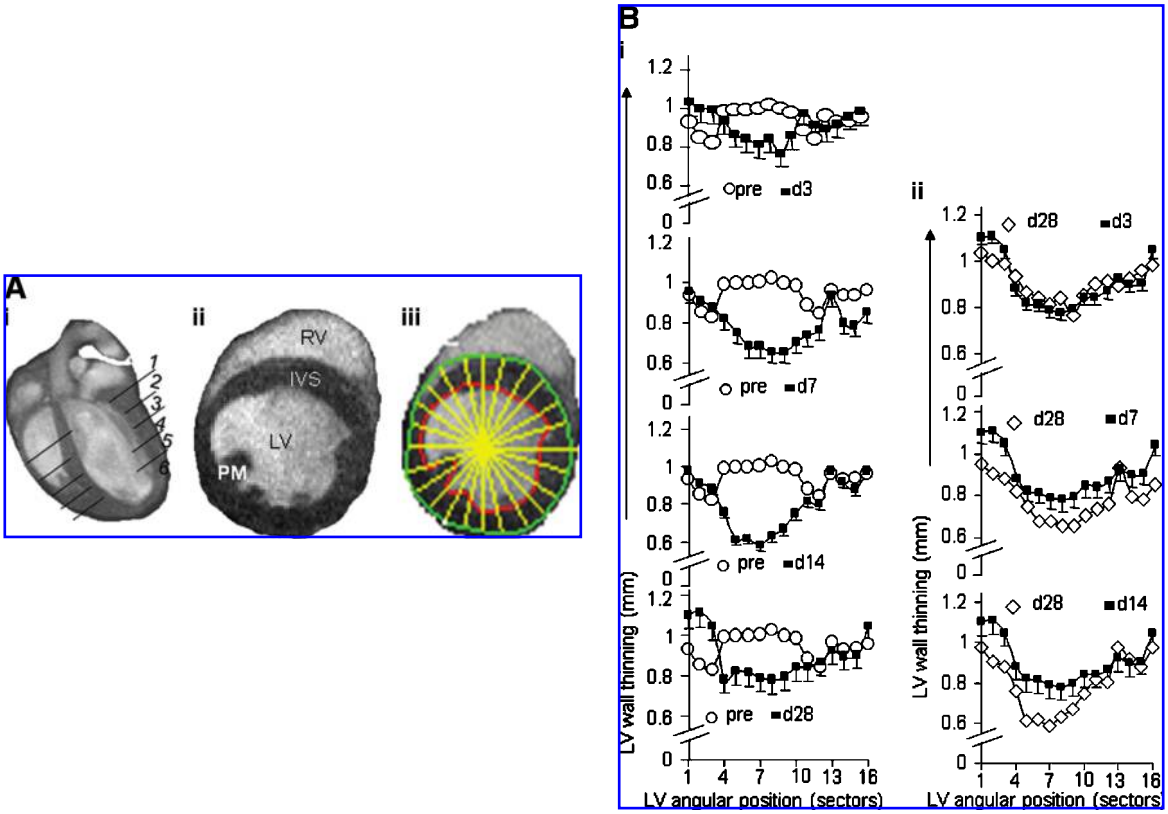

FIG. 2. Segmental measurement of wall-motion abnormality to assess anatomic remodeling of ischemia/reperfused murine heart. (**A**) (**i**) Representative long-axis image of a baseline mouse heart with a schematic depiction of the six imaging planes studied. The actual planes studied covered the entire LV long axis, enabling LV mass and volume calculation at the base; (**ii**) typical representative short-axis image obtained from the apical half of the LV; (**iii**) demarcation of sectors for wall-thickness measurements. Images with maximal infarction at the region below LAD occlusion for all time points were processed. LV epi- and endocardial borders and radial lines were drawn as shown. All pre- and postischemic images were processed based on the radii as reference lines to measure the wall thickness. LV was divided into 18 sectors (each 20 degrees) starting from the right ventricular corner as sector 1, with all other equal sectors rotating anticlockwise. The thicknesses of the wall at each radial line were measured by using Segment software. LV, left ventricle; RV, right ventricle; PM, papillary muscle; IVS, interventricular septum. (**B**) Post-IR wall thinning. Significant LV wall thinning caused by IR injury (sectors from 4 to 10) is observed. Post-IR wall-thickness data measured at different time points were compared with pre-IR data (left column, **i**) and post-IR day28 (right column, **ii**). Optimal compromised wall motion was observed on day 7 and day 14. Data represent mean ± SEM. Statistical treatment of data is presented in Table 3. (For interpretation of the references to color in this figure legend, the reader is referred to the web version of this article at www.liebertonline.com/ars).

Infarct patch–area analysis. Signal intensity was measured in the normal region of the myocardium, and mean ± SD was calculated. To determine hyperenhanced zones, we defined regions with image intensities greater than the mean signal intensity of the normal region within the transient and permanent infarct territories. If hyperenhancement was present, image intensities were thresholded at a level equal to 2 SD above the mean of the normal region and outlined only the hyperenhancement region to account for nontransmural involvement. The criterion for the threshold was chosen such that the "bright in the infarct is dead" (20). Contrast-enhanced short-axis images of the apical lower half of the LV with total infarct, magnified infarct region, and scar patches at different intensity levels were obtained by using these criteria. The delayed-hyperenhanced regions were subjected to contouring to detect the area of individual patchy islands. The necrotic and reversibly infarcted areas were quantified with planimetry.

Transmurality analysis. The transmural extent of infarction (transmurality) was computed for each segment as the ratio of hyperenhanced to nonhyperenhanced areas, as shown in Fig. 6. Average transmurality for each infarct was calculated as the average of all segments with transmurality greater than zero.

Statistical analyses

Data are presented as mean ± SEM. Significance of difference between means was determined (SPSS software package) with one-way analysis of variance (ANOVA) by using Tukey pairwise comparisons to assess differences between time points. Individual slices were considered to be separate observations (36). Student's paired *t* test was used to compare differences in transmurality in post-IR d3 and d28 (Fig. 6).

Results

LV function and mass

Attenuated R-wave amplitude, marked ST-segment elevation, and development of a large Q-wave were hallmarks of

Table 2. Sector-wise Diastolic Mean Wall Thickness (in mm) Following Ischemia/Reperfusion

# of Sectors	pre-IR	d3	d7	d14	d28
1	0.931595	1.033396	0.953974	0.975056	1.101323
2	0.852572	0.997633	0.905107	0.90879	1.108634
3	0.82386	0.98937	0.880231	0.881996	1.046132
4	0.986903	0.935859	0.818781	0.757131	0.881652
5	0.996074	0.865452	0.750749	0.610858	0.820135
6	0.995524	0.839362	0.676961	0.620387	0.814028
7	1.000417	0.811848	0.677347	0.582921	0.787473
8	1.024419	0.84299	0.6526	0.630149	0.777751
9	0.997985	0.767196	0.655264	0.66597	0.795837
10	0.982131	0.854038	0.701213	0.745519	0.843884
11	0.883158	0.902111	0.73539	0.814041	0.842338
12	0.843916	0.911095	0.761959	0.803375	0.868553
13	0.960949	0.89578	0.930933	0.976098	0.922397
14	0.929974	0.921196	0.796173	0.918665	0.897535
15	0.936043	0.96056	0.780904	0.877941	0.905034
16	0.929974	0.921196	0.796173	0.918665	0.897535
17	0.926043	0.95056	0.770904	0.867941	0.895034
18	0.947729	0.974049	0.839618	0.965841	1.034308

successful LAD occlusion during surgery. IR-insult compromised LV contraction, as manifested by enlarged end-diastole and end-systole volumes (Fig. 1A). Because our aim was to study remodeling in the surviving heart, myocardial infarction was limited to being mild. Under such conditions, EDV practically remained unchanged over time after IR. IR rapidly decreased stroke volume, and compromised stroke volume persisted over the duration of the study (Fig. 1Bi). Consistent with this observation, IR rapidly compromised LV functions, as represented by LVEF as well as CO (Fig. 1Bii). Concomitant with IR-induced rapid loss of LV function, LV mass substantially increased. This change was most prominent on day 3 after IR. This observation may have been contributed by edema in the inflammation phase or acute cardiomyocyte hypertrophy or both. As a function of recovery time, IR-induced increase in LV mass was noted to decrease. Although LV mass on post-IR day 28 was significantly higher than pre-IR baseline values, it was also significantly lower than the LV mass noted on post-IR day 3 (Fig. 1Biii; Table 1).

Table 3. Statistical Treatment for Fig. 2B Addressing Cardiac Wall-motion Abnormality

pre-IR vs d3	ns
pre-IR vs d7	***
pre-IR vs d14	**
pre-IR vs d28	ns
d3 vs d7	**
d3 vs d14	*
d3 vs d28	ns
d7 vs d14	ns
d7 vs d28	*
d14 vs d28	*

*$p < 0.05$.
**$p < 0.01$.
***$p < 0.001$.
ns, not significant different.

LV wall-motion abnormality

A segmental approach to measure LV wall motion was adopted (Fig. 2A). IR compromised LV contractility and caused enlargement of the cavity. IR-induced wall thinning was specifically noted in the anterior aspect of the LV, as represented by the angular positions 4 through 10. Unlike changes in LV function and mass that were most prominently noted on day 3 after IR, the LV wall-thinning response was most marked in post-IR days 7 and 14. In the border-zone sectors encompassing the midventricular and apical anterior septum, which were adjacent to infarcted anterior sectors, marginal decline of wall thickness was noted on post-IR day 3 (see data, Table 2). Such wall-thinning response, however, was significant on post-IR days 7 and 14. Recovery of wall thickness in these segments was noted in post-IR day 28. In the sector representing the midventricular septum, located remote from the infarct site, no significant change in wall motion was noted (Table 3).

Infarct volume

The time course of hyperenhancement of LV injury was assessed by using the MR inversion-recovery sequence, which recognized true infarct size (Fig. 3). Earliest contrast-enhanced images were obtained 20–30 min after contrast administration. Consistent with IR-induced changes noted in LV mass and function, infarct size was observed to be the largest on post-IR days 3 and 7. With time, however, the infarct size significantly decreased (Fig. 3, Table 3). Pixel-wise analysis of delayed hyperenhancement of infarct region *via* signal intensity was performed for the assessment of ischemic severity. A typical four-chamber view of the infarcted heart on post-IR day 3 is shown Fig. 4i. A representative contrast-enhanced short-axis image of the apical half of the LV depicting the injury on post-IR day 3 is presented in Fig. 4ii. Both normal (x) and hyperenhanced (y) regions were analyzed to obtain intensities of the normal myocardium and hyperenhanced myocardium, respectively. We observed that IR-induced absolute signal-intensity enhancement was highest on post-IR days 3 and 7. As a function of post-IR time, the signal-intensity enhancement was attenuated, suggesting that some of the damaged tissue may have recovered or the formation of scar tissue that does not lend itself to Gd-DTPA access because of compromised vascularization or both.

Infarct patch area analysis

The hyperenhanced region was thresholded to obtain image intensities at three different regions: the normal myocardium, myocardium transient to infarction, and permanent infarction (24). Representative contrast-enhanced short-axis images of apical lower-half of LV depicting the total infarct, magnified infarct region, and scar patches at different intensity levels are shown in Fig. 5. The delayed-hyperenhanced regions are shown by contours. The necrotic and reversibly infarcted areas are quantitatively illustrated in Fig. 5iii (36). Interestingly, although the necrotic tissue area remains unaltered during the course of the post-IR recovery period, the reversibly infarcted tissue markedly was minimized during 4 weeks of recovery (Fig. 5iii).

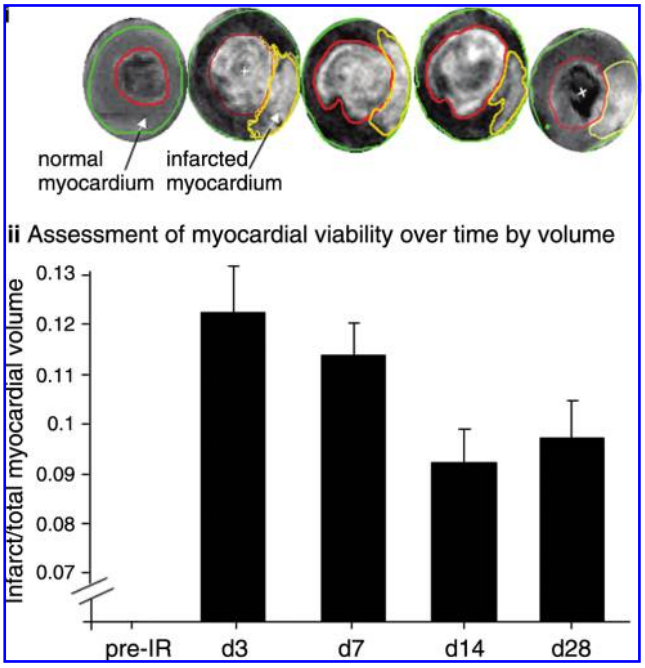

FIG. 3. Infarct size after ischemia/reperfusion. Contrast enhancement after Gd-DTPA injection at different time points after IR. T_1 weighting was achieved with an inversion-recovery fast low-angle shot (ir-FLASH) pulse sequence (TE = 30 ms; TR = 1,000 ms; matrix size = 256×192 mm; TI = 275 ms; FA = 60 degrees). Images were acquired during breath-hold (acquiring images within short acquisition times, which produced images that were comparatively free of motional artifact from cardiac or respiratory movement) (8 s) and were ECG gated to end systole to achieve contrast caused hyperenhancement between normal and injured tissue. (**i**) Representative epi- and endocardial borders and infarct contours were drawn by using Segment software for all time points (see time-point label for ii vertically below). The area of hyperenhanced injury was obtained by planimetry on two to three slices, depending on the infarct size and location and by applying Simson's rule. Infarct volume was calculated by multiplying the total area by the slice thickness; Note: image quality is poorer at the apex because of motion. Therefore, mid-LV slices are shown for the sake of better image quality. (**ii**) Changes in infarct size over time. The ratio of infarct volume to normal LV myocardial volume was plotted over time. Data represent mean ± SEM. Statistical treatment of data is presented in Table 4. T_1, tissue magnetization recovery time; TI, inversion recovery time; LV, left ventricle; TR, repetition time; TE, echo time; FA, flip angle; IR, ischemia/reperfusion; Gd DTPA, gadolinium diethylenetriamine pentaacetic acid. (For interpretation of the references to color in this figure legend, the reader is referred to the web version of this article at www.liebertonline.com/ars).

Transmurality analysis

The average transmurality of each infarct was calculated as the average of all segments with evidence of transmurality (Fig. 6). Delayed contrast-enhanced images obtained by administering Gd-DTPA to mice at different time points after IR were processed for the calculation of hyperenhanced and nonhyperenhanced patch areas of myocardium for all affected slices. Transmurality was expressed as a ratio of mean hyperenhanced to mean nonhyperenhanced areas (34). The approach adopted in this study was able to track infarct transmurality in beating murine hearts subjected to IR. Infarct transmurality markedly increased during post-IR recovery (day 3 *vs*. day 28), indicating that the permanent injury remains unchanged, whereas part of the reversibly injured tissue recovers in 4 weeks after IR.

Table 4. Statistical Treatment for Fig. 3ii Addressing Cardiac Infarct Size

pre-IR vs d3	**
pre-IR vs d7	**
pre-IR vs d14	**
pre-IR vs d28	**
d3 vs d7	ns
d3 vs d14	*
d3 vs d28	*
d7 vs d14	*
d7 vs d28	*
d14 vs d28	ns

*$p < 0.05$.
**$p < 0.01$.
ns, not significant different.

Discussion

Increased end-diastolic volume and compromised contractile function are commonly noted in the IR heart (50). Our observations are consistent with the literature demonstrating that after IR, cardiac functions are compromised and remain so over time (3, 17, 50). Attenuated LV ejection fraction and cardiac output in the post-IR heart represent hallmarks of a compromised state of cardiac function (41). Left ventricular hypertrophy, as is noted after myocardial infarction (2, 30, 46), was observed as an acute response after IR. Interestingly, during the four weeks of recovery after IR, although LV hypertrophy was still evident, LV mass was significantly lower compared with results recorded on post-IR day 3. Abnormal regional wall motion after myocardial infarction is caused by disrupted perfusion of the affected sites (11). LV segmental wall motion is useful to assess overall left ventricular function in acute myocardial infarction (22). Consistent with the clinical literature (1), we observed a gradation of wall-motion abnormality that consisted of hypokinetic (thinning, 40–50%) and akinetic (thinning, 30–40%) components. Progressive worsening of wall motion was noted during the first 2 weeks after IR. This is consistent with the notion of progressive myocyte death in the IR-affected myocardial site (33). In all middle and apical slices, the circumferential extent of wall thinning progressively increased in regions at angular positions 4 through 10. Analysis of the midventricular slices revealed that it was not only the IR-affected site where wall thinning was evident but also the wall diametrically opposite the infarct site had the thinning response. This response, although not clearly evident on post-IR day 3, was significantly noted on post-IR day 7. Mechanical load on the remote wall caused by the malfunctioning infarct site is likely to be responsible for the observation. Longitudinal measures conducted in our study demonstrate that in the murine heart, the thinning response is a progressive process that seems to peak on post-IR days 7 to 14. Beyond the first 2 weeks of IR, the structural geometry of the heart suggests that the thinning response not only stops but also partly reverses, as noted on

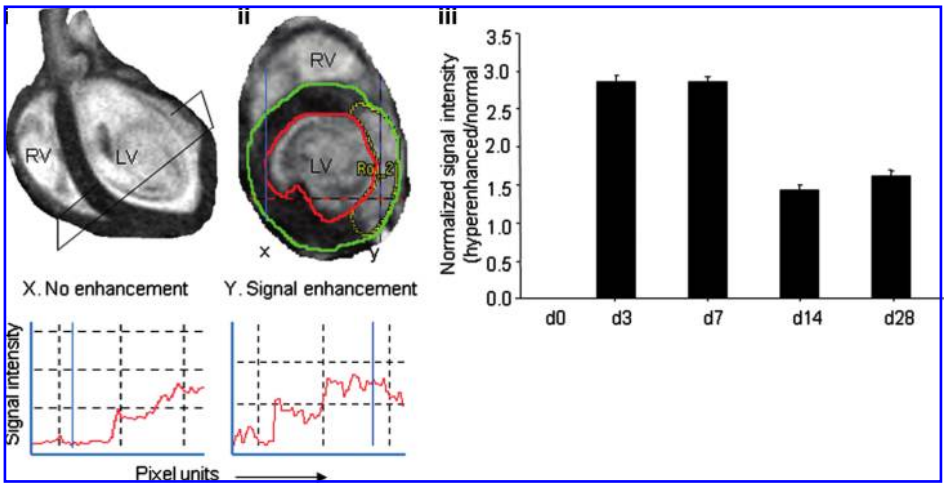

FIG. 4. Pixel-wise analysis of delayed hyperenhancement of infarct region. (**i**) Typical four-chamber view of infarcted heart (post-IR day 3). (**ii**) Representative contrast-enhanced short-axis image at apical half of LV depicting the injury on post-IR day 3. (**iii**) Quantitative data from images processed by using Para-Vision PV4.0 (Bruker, Ettlingen, Germany) software for intensity analysis. Both normal and hyperenhanced regions were analyzed to obtain intensities of the normal myocardium (x) and hyperenhanced myocardium (y) by using the pixel-scan option. *Bottom left*, signal-intensity profile for the normal myocardium (x). *Bottom right*, signal-intensity profile for the infarcted myocardium (y). Data represent mean ± SEM. Statistical treatment of data is presented in Table 5. (For interpretation of the references to color in this figure legend, the reader is referred to the web version of this article at www.liebertonline.com/ars).

post-IR day 28. Contribution of the scar tissue to this reversal response is likely, and histologic characterization is therefore of interest.

Clinically, hyperenhancement is commonly noted in post-IR myocardium after Gd-DTPA administration (31). Double-inversion pulse to null blood signal enhanced the contrast-to-noise ratio. Gd-DTPA rapidly diffuses out of capillaries into the extracellular space but cannot cross intact cell membranes. At the site of injury, however, Gd-DTPA enters into cells with compromised membrane integrity and is retained at that location because of poor perfusion of the injured tissue (45, 47). Partial-volume effect in the injured myocardium adds a layer of complexity to this interpretation (18, 23, 24). The partial-volume effect represents any of a set of effects that occur due to the finite size of the detection elements or resolution elements (voxels) and the fact that the object structure may vary rapidly over the region. When the object varies rapidly over distances comparable to the spatial resolution, one expects the image value to reflect the average value over the resolution element. This partial-volume averaging, a manifestation of the limited spatial resolution, is also called the linear partial-volume effect. Prudent consideration of the partial-volume effect is critical to the rational interpretation of MRI observations (27). We observed that the absolute volume of hyperenhanced myocardium decreased by a factor of 3.6 between post-IR days 3 and 28. Hyperenhancement includes both acutely necrotic regions and surrounding reversibly injured regions (10), as presented on post-IR day 3. Over the 4-week period of post-IR recovery, the necrotic tissue cannot reverse into viable myocardium, but a fraction of the reversibly injured tissue does recover, fractionally attenuating the infarct size. We also noted that the spatial extent of post-IR scar at 4 weeks of recovery was 3.6 times smaller than the spatial extent of acute myocyte necrosis at post-IR day 3. In canines, it is known that the infarct shrinks fourfold between post-IR day 4 and 6 weeks (30, 37). This is consistent with our observation demonstrating a significant reduction of proportional infarct size during 4 weeks of post-IR recovery. The observed reduction of infarct size over a 4-week period of post-IR recovery may be explained by (a) replacement of necrotic tissue by scar tissue (6, 9, 16, 28, 32), and (b) compensatory hypertrophy or enlargement of the uninjured tissue, with the goal to preserve cardiac function in the insulted heart (44).

Transmural ischemia is said to exist when ischemia extends subepicardially. This process has a more-visible effect on recovery of subepicardial cells compared with subendocardial cells. Recovery is more delayed in the subepicardial layers, and the subendocardial muscle fibers seem to recover first. Delayed contrast-enhanced cardiac MRI allows the direct visualization of the transmural extent of scar at high spatial resolution. This work provides a validated methodologic approach that is useful to quantify post-IR infarct tissue. When imaged by adopting a DHE MRI technique with an inversion-prepared T_1-weighted sequence after injection of gadolinium chelates, the infarcted myocardium appears hyperenhanced relative to the unaffected healthy myocardium. The transmural extent of DHE predicts functional and anatomic remodeling in acute myocardial infarction as well as in chronic ischemic heart disease (7, 32, 34, 40). This approach can accurately discriminate between infarcted

Table 5. Statistical Treatment for Fig. 4Aiii Addressing Delayed Hyperenhancement of Cardiac Infarct Tissue

pre-IR vs d3	***
pre-IR vs d7	***
pre-IR vs d14	***
pre-IR vs d28	***
d3 vs d7	ns
d3 vs d14	*
d3 vs d28	*
d7 vs d14	*
d7 vs d28	*
d14 vs d28	ns

*$p < 0.05$.
***$p < 0.001$.
ns, not significant different.

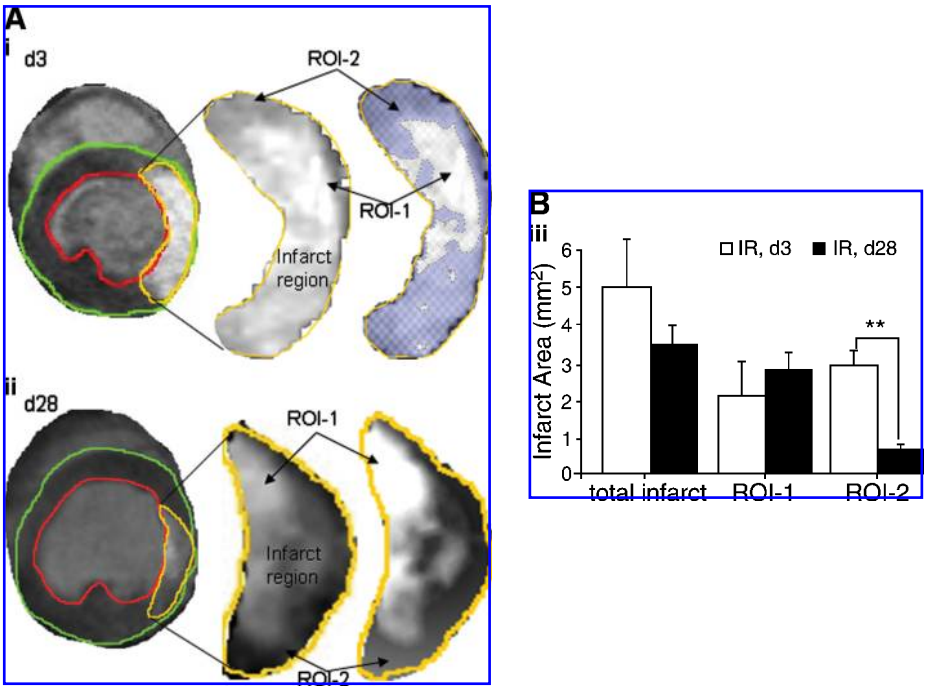

FIG. 5. Analysis of delayed hyperenhanced infarct patchy-scar area. Delayed contrast–enhancement MR imaging was performed on mice injected with Gd-DTPA. Contrast-enhanced pixel-wise analysis was performed. Representative contrast-enhanced short axis image at the apical half of the LV depicting the injury (infarct region), magnified version of the infarct (ROI-2), and scar patches of different intensity values thresholded from the infarct region (ROI-1) at post-IR day3 (**i**) and day 28 (**ii**) (**A**). The delayed-hyperenhanced region is shown by contours. Hyperenhanced regions were thresholded to obtain image intensities at three different regions: normal myocardium, myocardium transient to occlusion, and permanent occlusion. (**B**) (**iii**) Bar graphs illustrate total infarct area, scar area, and reversibly infarcted area. Data represent mean ± SEM. $^{*}p < 0.05$; $^{**}p < 0.01$. ROI, region of interest; ROI-1, necrotic tissue or bona fide infarct tissue; ROI-2, reversibly infarcted tissue. (For interpretation of the references to color in this figure legend, the reader is referred to the web version of this article at www.liebertonline.com/ars).

and dysfunctional but viable myocardium. The extent of delayed enhancement is reproducible and closely correlates with the size of myocardial necrosis or infarct scar (40). The transmural extent of viable tissue is inversely proportional to infarct expansion and may protect from subsequent LV remodeling (14). This work provides the first evidence from the study of transmurality in the post-IR heart of mice by using an 11.7-T system. Our observations are in tight agreement with clinical results addressing the key significance of scar size in LV remodeling (21, 34). Previously, it was suggested that contrast-enhanced MRI overestimates the size of myocardial infarcts when images are acquired much less than 20 min after contrast injection (24). We observed that chronic infarct or scar volume, assessed by MRI, remained practically constant from post-IR day 3 (2.09 mm^3) to day 28 (2.76 mm^3). However, IR-induced change in volume of the injured-tissue compartment represented by moderate gadolinium concentration was reversible (post-IR day 3, 2.90 mm^3; day 28, 0.66 mm^3). Understanding the biology of these patches of repairing infarct tissue by using laser capture microdissection approaches (25, 26, 39) is likely to provide major advances in our understanding of post-IR myocardial wound healing.

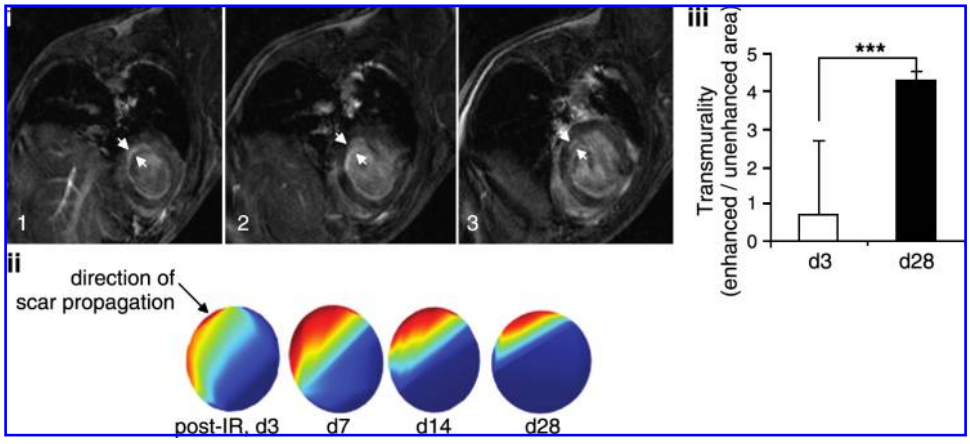

FIG. 6. Assessment of infarct transmurality. Delayed-contrast enhancement MR imaging was performed on mice injected with Gd-DTPA. Images were processed for the calculation of hyperenhanced and nonhyperenhanced infarct patch areas for all affected slices. (**i**) Axial image montage illustrating hyperenhanced LV myocardium. Only three (1–3) of six slices of slice thickness 1.2 mm were affected by IR. Thresholds for enhanced and nonenhanced patches areas were calculated. Transmurality was expressed as a ratio of mean hyperenhanced to mean nonhyperenhanced area; (**ii**) the direction of propagation of scar is shown (cyan edge) as spatial percentage maximum scar transmurality, estimated by using Segment software; (**iii**) results of scar transmurality on post-IR days 3 and 28 are illustrated. Data represent mean ± SEM. $^{***}p < 0.001$. (For interpretation of the references to color in this figure legend, the reader is referred to the web version of this article at www.liebertonline.com/ars).

Acknowledgments

This work was supported by NHLBI R01 HL073087.

Abbreviations

2Ch, two chamber; 4Ch, four chamber; CO, cardiac output; DCE, delayed contrast enhancement; DICOM, digital imaging and communications in medicine; EF, ejection fraction; FA, flip angle; FLASH, fast low-angle shot; FOV, field of view; Gd-DTPA, gadolinium diethylenetriamine pentaacetic acid; GRE, gradient-recalled echo; IR, ischemia/reperfusion; IVS, interventricular septum; LAD, left anterior descending artery; LV, left ventricle; MR, magnetic resonance; MRI, magnetic resonance imaging; PM, papillary muscle; ROI, region of interest; RV, right ventricle; SNR, signal-to-noise ratio; T_1, tissue magnetization recovery time; TE, echo time; TI, inversion-recovery time; TR, repetition time; SD, standard deviation.

Author Disclosure Statement

No competing financial interests exist.

References

1. Barbier CE, Bjerner T, Johansson L, Lind L, and Ahlstrom H. Myocardial scars more frequent than expected: magnetic resonance imaging detects potential risk group. *J Am Coll Cardiol* 48: 765–771, 2006.
2. Barrabes JA, Figueras J, Cortadellas J, Lidon RM, and Ibars S. Usefulness of electrocardiographic and echocardiographic left ventricular hypertrophy to predict adverse events in patients with a first non-ST-elevation acute myocardial infarction. *Am J Cardiol* 103: 455–460, 2009.
3. Bello D, Shah DJ, Farah GM, Di Luzio S, Parker M, Johnson MR, Cotts WG, Klocke FJ, Bonow RO, Judd RM, Gheorghiade M, and Kim RJ. Gadolinium cardiovascular magnetic resonance predicts reversible myocardial dysfunction and remodeling in patients with heart failure undergoing beta-blocker therapy. *Circulation* 108: 1945–1953, 2003.
4. Bondarenko O, Beek AM, Twisk JW, Visser CA, and van Rossum AC. Time course of functional recovery after revascularization of hibernating myocardium: a contrast-enhanced cardiovascular magnetic resonance study. *Eur Heart J* 29: 2000–2005, 2008.
5. Bundschuh CV, Stein L, Slusser JH, Schinco FP, Ladaga LE, and Dillon JD. Distinguishing between scar and recurrent herniated disk in postoperative patients: value of contrast-enhanced CT and MR imaging. *AJNR Am J Neuroradiol* 11: 949–958, 1990.
6. Catalano O, Antonaci S, Moro G, Cannizzaro G, Mingrone R, Opasich C, Frascaroli M, Rognone F, Baldi M, and Tramarin R. Contrast-enhanced magnetic resonance imaging assessment of scar size in patients with chronic myocardial infarction. *Ital Heart J* 6: 133–137, 2005.
7. Chan J, Khafagi F, Young AA, Cowan BR, Thompson C, and Marwick TH. Impact of coronary revascularization and transmural extent of scar on regional left ventricular remodelling. *Eur Heart J* 29: 1608–1617, 2008.
8. Chapon C, Herlihy AH, and Bhakoo KK. Assessment of myocardial infarction in mice by late gadolinium enhancement MR imaging using an inversion recovery pulse sequence at 9.4T. *J Cardiovasc Magn Reson* 10: 6, 2008.
9. Choi BW. Differentiation of acute myocardial infarction from chronic myocardial scar with MRI. *Korean J Radiol* 7: 1–3, 2006.
10. Egred M, Al-Mohammad A, Waiter GD, Redpath TW, Semple SK, Norton M, Welch A, and Walton S. Detection of scarred and viable myocardium using a new magnetic resonance imaging technique: blood oxygen level dependent (BOLD) MRI. *Heart* 89: 738–744, 2003.
11. Feigenbaum H. *Feigenbaum's echocardiography*. 6th ed. New York: Lippincott Williams and Wilkins, 2005.
12. Gilson WD, Epstein FH, Yang Z, Xu Y, Prasad KM, Toufektsian MC, Laubach VE, and French BA. Border zone contractile dysfunction is transiently attenuated and left ventricular structural remodeling is markedly reduced following reperfused myocardial infarction in inducible nitric oxide synthase knockout mice. *J Am Coll Cardiol* 50: 1799–1807, 2007.
13. Gilson WD and Kraitchman DL. Cardiac magnetic resonance imaging in small rodents using clinical 1.5 T and 3.0 T scanners. *Methods* 43: 35–45, 2007.
14. Haughton V, Schreibman K, and De Smet A. Contrast between scar and recurrent herniated disk on contrast-enhanced MR images. *AJNR Am J Neuroradiol* 23: 1652–1656, 2002.
15. Heiberg E, Engblom H, Engvall J, Hedstrom E, Ugander M, and Arheden H. Semi-automatic quantification of myocardial infarction from delayed contrast enhanced magnetic resonance imaging. *Scand Cardiovasc J* 39: 267–275, 2005.
16. Helm PA, Caravan P, French BA, Jacques V, Shen L, Xu Y, Beyers RJ, Roy RJ, Kramer CM, and Epstein FH. Post-infarction myocardial scarring in mice: molecular MR imaging with use of a collagen-targeting contrast agent. *Radiology* 247: 788–796, 2008.
17. Hendrikx M, Hensen K, Clijsters C, Jongen H, Koninckx R, Bijnens E, Ingels M, Jacobs A, Geukens R, Dendale P, Vijgen J, Dilling D, Steels P, Mees U, and Rummens JL. Recovery of regional but not global contractile function by the direct intramyocardial autologous bone marrow transplantation: results from a randomized controlled clinical trial. *Circulation* 114: I101–107, 2006.
18. Hunold P, Schlosser T, Vogt FM, Eggebrecht H, Schmermund A, Bruder O, Schuler WO, and Barkhausen J. Myocardial late enhancement in contrast-enhanced cardiac MRI: distinction between infarction scar and non-infarction-related disease. *AJR Am J Roentgenol* 184: 1420–1426, 2005.
19. Isbell DC and Kramer CM. Cardiovascular magnetic resonance: structure, function, perfusion, and viability. *J Nucl Cardiol* 12: 324–336, 2005.
20. Judd RM, Wagner A, Rehwald WG, Albert T, and Kim RJ. Technology insight: assessment of myocardial viability by delayed-enhancement magnetic resonance imaging. *Nat Clin Pract Cardiovasc Med* 2: 150–158, 2005.
21. Kaandorp TA, Lamb HJ, Viergever EP, Poldermans D, Boersma E, van der Wall EE, de Roos A, and Bax JJ. Scar tissue on contrast-enhanced MRI predicts left ventricular remodelling after acute infarction. *Heart* 93: 375–376, 2007.
22. Kan G, Visser CA, Koolen JJ, and Dunning AJ. Short and long term predictive value of admission wall motion score in acute myocardial infarction: a cross sectional echocardiographic study of 345 patients. *Br Heart J* 56: 422–427, 1986.
23. Kim KA, Seo JB, Do KH, Heo JN, Lee YK, Song JW, Lee JS, Song KS, and Lim TH. Differentiation of recently infarcted myocardium from chronic myocardial scar: the value of contrast-enhanced SSFP-based cine MR imaging. *Korean J Radiol* 7: 14–19, 2006.
24. Kim RJ, Fieno DS, Parrish TB, Harris K, Chen EL, Simonetti O, Bundy J, Finn JP, Klocke FJ, and Judd RM. Relationship of MRI delayed contrast enhancement to irreversible injury, infarct age, and contractile function. *Circulation* 100: 1992–2002, 1999.

25. Kuhn DE, Roy S, Radtke J, Gupta S, and Sen CK. Laser microdissection and pressure-catapulting technique to study gene expression in the reoxygenated myocardium. *Am J Physiol Heart Circ Physiol* 290: H2625–H2632, 2006.
26. Kuhn DE, Roy S, Radtke J, Khanna S, and Sen CK. Laser microdissection and capture of pure cardiomyocytes and fibroblasts from infarcted heart regions: perceived hyperoxia induces p21 in peri-infarct myocytes. *Am J Physiol Heart Circ Physiol* 292: H1245–H1253, 2007.
27. Kwong RY, Chan AK, Brown KA, Chan CW, Reynolds HG, Tsang S, and Davis RB. Impact of unrecognized myocardial scar detected by cardiac magnetic resonance imaging on event-free survival in patients presenting with signs or symptoms of coronary artery disease. *Circulation* 113: 2733–2743, 2006.
28. Kwong RY and Korlakunta H. Diagnostic and prognostic value of cardiac magnetic resonance imaging in assessing myocardial viability. *Top Magn Reson Imaging* 19: 15–24, 2008.
29. McNamara MT and Higgins CB. Magnetic resonance imaging of chronic myocardial infarcts in man. *AJR Am J Roentgenol* 146: 315–320, 1986.
30. McNamara MT, Higgins CB, Schechtmann N, Botvinick E, Lipton MJ, Chatterjee K, and Amparo EG. Detection and characterization of acute myocardial infarction in man with use of gated magnetic resonance. *Circulation* 71: 717–724, 1985.
31. Nieman K, Shapiro MD, Ferencik M, Nomura CH, Abbara S, Hoffmann U, Gold HK, Jang IK, Brady TJ, and Cury RC. Reperfused myocardial infarction: contrast-enhanced 64-section CT in comparison to MR imaging. *Radiology* 247: 49–56, 2008.
32. Oh YS, Thomson LE, Fishbein MC, Berman DS, Sharifi B, and Chen PS. Scar formation after ischemic myocardial injury in MRL mice. *Cardiovasc Pathol* 13: 203–206, 2004.
33. Ojha N, Roy S, Radtke J, Simonetti O, Gnyawali S, Zweier JL, Kuppusamy P, and Sen CK. Characterization of the structural and functional changes in the myocardium following focal ischemia-reperfusion injury. *Am J Physiol Heart Circ Physiol* 294: H2435–H2443, 2008.
34. Orn S, Manhenke C, Anand IS, Squire I, Nagel E, Edvardsen T, and Dickstein K. Effect of left ventricular scar size, location, and transmurality on left ventricular remodeling with healed myocardial infarction. *Am J Cardiol* 99: 1109–1114, 2007.
35. Raman SV, Richards DR, Jekic M, Dickerson JA, Kander NH, Foster EL, and Simonetti OP. Treadmill stress cardiac magnetic resonance imaging: first *in vivo* demonstration of exercise-induced apical ballooning. *J Am Coll Cardiol* 52: 1884, 2008.
36. Raman SV, Simonetti OP, Cataland SR, and Kraut EH. Myocardial ischemia and right ventricular dysfunction in adult patients with sickle cell disease. *Haematologica* 91: 1329–1335, 2006.
37. Reimer KA and Jennings RB. Failure of the xanthine oxidase inhibitor allopurinol to limit infarct size after ischemia and reperfusion in dogs. *Circulation* 71: 1069–1075, 1985.
38. Roy S, Khanna S, Hussain SR, Biswas S, Azad A, Rink C, Gnyawali S, Shilo S, Nuovo GJ, and Sen CK. MicroRNA expression in response to murine myocardial infarction: miR-21 regulates fibroblast metalloprotease-2 *via* phosphatase and tensin homologue. *Cardiovasc Res* 82: 21–29, 2009.
39. Roy S, Khanna S, Rink T, Radtke J, Williams WT, Biswas S, Schnitt R, Strauch AR, and Sen CK. P21waf1/cip1/sdi1 as a central regulator of inducible smooth muscle actin expression and differentiation of cardiac fibroblasts to myofibroblasts. *Mol Biol Cell* 18: 4837–4846, 2007.
40. Saraste A, Nekolla S, and Schwaiger M. Contrast-enhanced magnetic resonance imaging in the assessment of myocardial infarction and viability. *J Nucl Cardiol* 15: 105–117, 2008.
41. Schvartzman PR, Srichai MB, Grimm RA, Obuchowski NA, Hammer DF, McCarthy PM, Kasper JM, and White RD. Nonstress delayed-enhancement magnetic resonance imaging of the myocardium predicts improvement of function after revascularization for chronic ischemic heart disease with left ventricular dysfunction. *Am Heart J* 146: 535–541, 2003.
42. Simonetti OP, Finn JP, White RD, Laub G, and Henry DA. "Black blood" T2-weighted inversion-recovery MR imaging of the heart. *Radiology* 199: 49–57, 1996.
43. Simonetti OP, Kim RJ, Fieno DS, Hillenbrand HB, Wu E, Bundy JM, Finn JP, and Judd RM. An improved MR imaging technique for the visualization of myocardial infarction. *Radiology* 218: 215–223, 2001.
44. Strzelczyk J and Attili A. Cardiac magnetic resonance evaluation of myocardial viability and ischemia. *Semin Roentgenol* 43: 193–203, 2008.
45. Tanabe K, Ishibashi Y, Shimada T, Tsukihashi H, Hatano J, Oyake N, Morioka S, Moriyama K, Sugimura K, Yuasa K, and Kawamitsu H. Evaluating coronary reperfusion during acute myocardial infarction in a canine model by gadolinium-DTPA-enhanced magnetic resonance imaging. *Jpn Circ J* 57: 458–466, 1993.
46. van Deel ED, Lu Z, Xu X, Zhu G, Hu X, Oury TD, Bache RJ, Duncker DJ, and Chen Y. Extracellular superoxide dismutase protects the heart against oxidative stress and hypertrophy after myocardial infarction. *Free Radic Biol Med* 44: 1305–1313, 2008.
47. Wang YN, Jin ZY, Zhang ZH, Kong LY, Chen LB, Zhou L, Sun HY, Zhang H, and Miao Q. Assessment of myocardial viability with contrast-enhanced magnetic resonance imaging and comparison with single-photon emission computed tomography. *Chin Med Sci J* 21: 239–244, 2006.
48. Wiesmann F, Ruff J, Engelhardt S, Hein L, Dienesch C, Leupold A, Illinger R, Frydrychowicz A, Hiller KH, Rommel E, Haase A, Lohse MJ, and Neubauer S. Dobutamine-stress magnetic resonance microimaging in mice: acute changes of cardiac geometry and function in normal and failing murine hearts. *Circ Res* 88: 563–569, 2001.
49. Yang Z, Berr SS, Gilson WD, Toufektsian MC, and French BA. Simultaneous evaluation of infarct size and cardiac function in intact mice by contrast-enhanced cardiac magnetic resonance imaging reveals contractile dysfunction in noninfarcted regions early after myocardial infarction. *Circulation* 109: 1161–1167, 2004.
50. Zhou R, Pickup S, Glickson JD, Scott CH, and Ferrari VA. Assessment of global and regional myocardial function in the mouse using cine and tagged MRI. *Magn Reson Med* 49: 760–764, 2003.

Address correspondence to:
Chandan K. Sen
512 Heart & Lung Research Institute
473 W. 12th Avenue
Columbus, OH 43210

E-mail: chandan.sen@osumc.edu

Date of first submission to ARS Central, April 20, 2009; date of final revised submission, May 18, 2009; date of acceptance, May 18, 2009.

This article has been cited by:

1. Daniel J Stuckey, Carolyn A Carr, Stephanie J Meader, Damian J Tyler, Mark A Cole, Kieran Clarke. 2011. First-pass perfusion CMR two days after infarction predicts severity of functional impairment six weeks later in the rat heart. *Journal of Cardiovascular Magnetic Resonance* **13**:1, 38. [CrossRef]
2. S. Roy, S. Khanna, A. Azad, R. Schnitt, G. He, C. Weigert, H. Ichijo, C. K. Sen. 2010. Fra-2 mediates oxygen-sensitive induction of transforming growth factor in cardiac fibroblasts. *Cardiovascular Research* **87**:4, 647-655. [CrossRef]